Supplemental Material for: Spectral shifts in tip-induced light from plasmonic nanoparticles in air

Mario Zapata-Herrera,[1] Benoît Rogez,[2,*] Sylvie Marguet,[3] Gérald Dujardin,[2] Elizabeth Boer-Duchemin,[2] and Eric Le Moal[2,†]

[1] *Donostia International Physics Center (DIPC), Donostia-San Sebastián 20018, Spain*
[2] *Université Paris-Saclay, CNRS, Institut des Sciences Moléculaires d'Orsay, 91405, Orsay, France*
[3] *Université Paris-Saclay, CEA, CNRS, NIMBE, 91191, Gif-sur-Yvette, France*

(Dated: April 5, 2024)

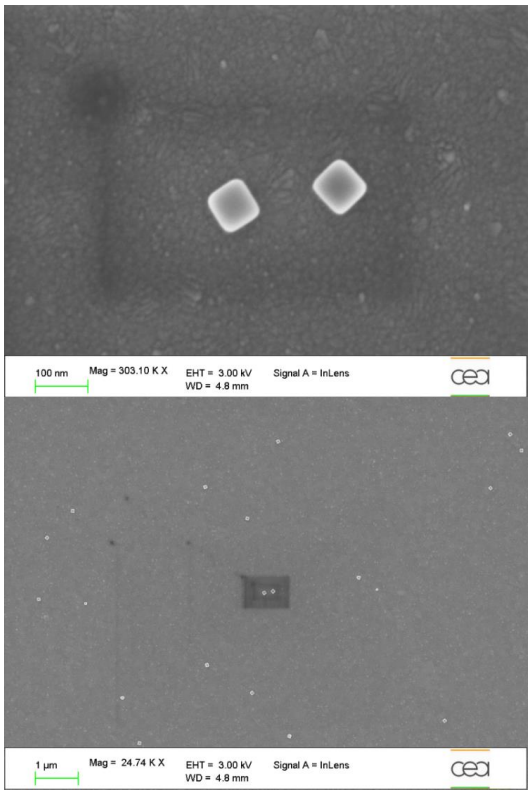

FIG. S1. Scanning electron micrographs (SEM) of plasmonic nanoparticles dispersed on a transparent conductive substrate, i.e., a glass coverslip coated with a 85 nm-thick indium-tin oxide (ITO) layer. The nanoparticles are chemically synthesized monocristalline gold nanocubes, 75 nm in edge length, with rounded edges and corners with typical radii of curvature of 10 nm (see also Refs. S1–S3). Top: SEM magnification ×303100, scale bar 100 nm. Bottom: SEM magnification ×24740, scale bar 1 μm.

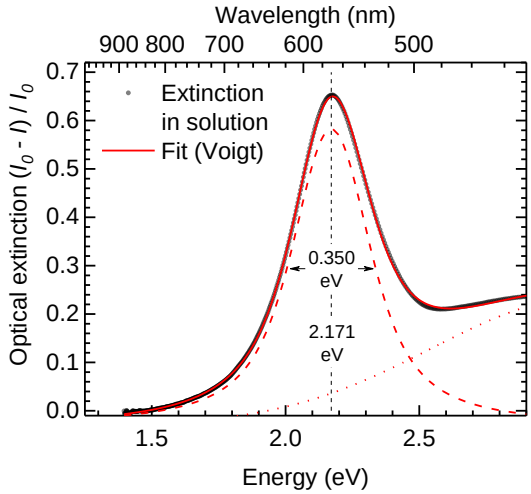

FIG. S2. Optical extinction spectrum measured in solution. The experimental data are fitted using Voigt profiles.

I. CHARACTERIZATION OF THE NANOPARTICLES

Figure S1 shows scanning electron micrographs (SEM) of plasmonic nanoparticles (NPs) from the sample used in this study.

Figure S2 shows an extinction spectrum measured in solution of the plasmonic NPs used in this study. The peak at 2.17 eV with a full width at half maximum (FWHM) of 0.35 eV is ascribed to the resonance of the energy-degenerate dipolar plasmon modes of the NPs. This peak is best fitted with the convolution (Voigt profile) of a Gaussian curve that has a FWHM of 0.18 eV and a Lorentzian curve that has a FWHM of 0.26 eV. As an approximation, we assume that the resonance of the dipolar plasmon modes of an individual NP has a Lorentzian profile and that the Gaussian contribution to the Voigt profile results from inhomogeneous broadening, e.g., due to the distribution of NP sizes in the solution. Thus, we estimate that the resonance of the dipolar plasmon modes of an individual NP has a FWHM of 0.26 eV.

* Present address: Laboratory Light, nanomaterials and nanotechnologies - L2n, University of Technology of Troyes - CNRS EMR 7004, 12 rue Marie Curie, 10000 Troyes, France
† eric.le-moal@universite-paris-saclay.fr

II. ANALYSIS OF FOURIER-SPACE IMAGES

Figure S3 shows a comparison of scanning tunneling microscope (STM)-induced luminescence (STML) measurements and numerical simulations where we consider a point-like oscillating electric dipole on an air-glass interface [S4, S5]. The Fourier-space optical microscopy images have been recorded during the excitation of a single gold nanocube with the STM tip located in the center of the cube's top face [see Fig. S3(a)] or on its corner [see Fig. S3(b)]. The experimental data shown in Figs. S3(a) and S3(b) are the same as the data shown in Figs. 2(f) and 2(g) of the main article. In order to reproduce these experimental data, Fourier-space images are simulated for the radiation pattern of a dipole oriented along the out-of-plane axis **z** [see Fig. S3(c)] and tilted with respect to **z** by an angle $\Theta = 25°$ in the **xz**-plane [see Fig. S3(d)]. Intensity profiles taken from Figs. S3(a) and S3(c) along the dotted line shown in Fig. S3(a) are plotted in Fig. S3(e). Intensity profiles taken from Figs. S3(b) and S3(d), as well as similar theoretical data calculated for $\Theta = 20°$ and $\Theta = 30°$, are plotted in Fig. S3(f).

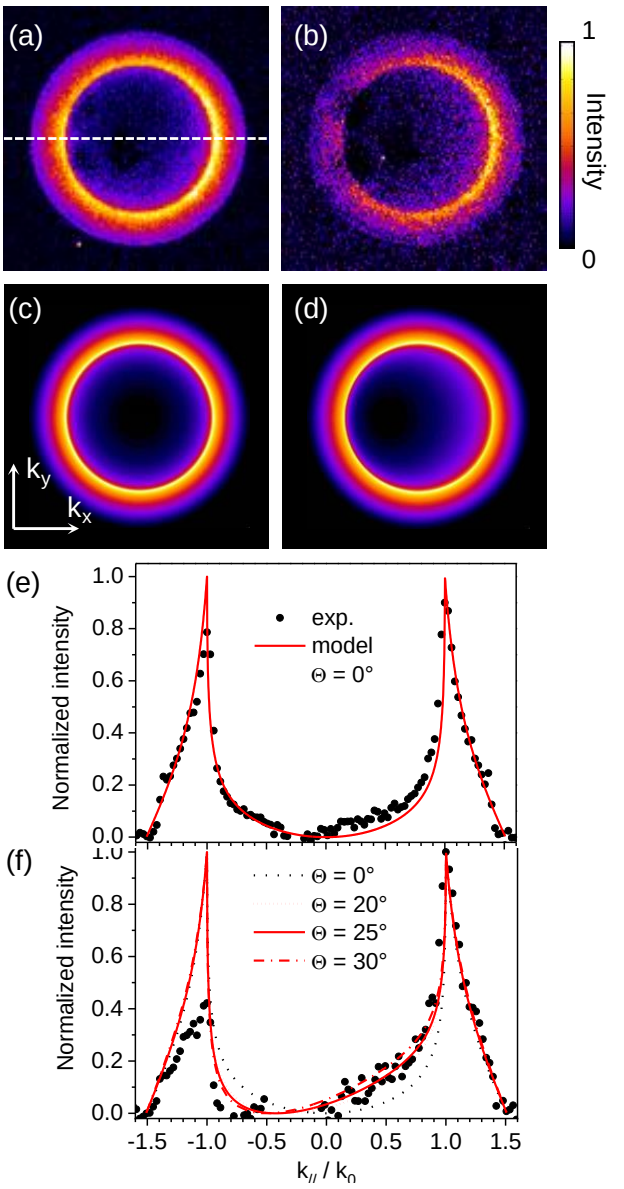

FIG. S3. STM-induced luminescence (STML) of a single gold nanocube: experiment and model. (a,b) Fourier-space optical microscopy images of the STML measured when the STM tip is (a) in the center or (b) on the corner of the cube's top face. (c,d) Simulated Fourier-space images obtained by calculating the radiation pattern of an oscillating electric dipole on an air-glass interface, where the dipole orientation is (c) parallel to the out-of-plane axis, i.e., $\Theta = 0°$, and (d) tilted with respect to this axis by an angle of $\Theta = 25°$. Intensity profiles taken from panels a to d, for the cases where the tip is (e) in the center and (f) on the corner of the cube's top face.

III. SUPPLEMENTARY NUMERICAL SIMULATIONS

In Figure S4(a), the extinction, scattering and absorption cross sections of the NP on a glass substrate are plotted versus photon energy. These data are calculated for plane wave illuminations with two different orientations. As shown in Fig. S4(b), *s* refers to normal incidence with $\mathbf{E} \parallel \mathbf{x}$; whereas, *p* refers to a grazing incidence (80° off the normal) with the electric field **E** parallel to the incidence plane (*yz*). Thus, the in-plane and out-of-plane resonances of the NP are probed. In Fig. S4(a), we observe in-plane and out-of-plane dipolar resonances (referred to as D in the figure) at 2.05 eV and 2.11 eV, with FWHM of 0.24 eV and 0.40 eV, respectively.

Figure S5 shows the theoretical charge density distributions of the gold nanocube under plane wave illumination when the incident electric field is oriented along the **x**-axis, numerically calculated for a photon energy of (a) 2.07 eV and (b) 2.37 eV. The charge distributions shown in Figs. S5(a) and S5(b) exhibit the typical symmetry of a dipolar and a quadrupolar plasmon mode, respectively. On the basis of these calculated charge distributions, the secondary absorption peak seen at 2.34 eV in Fig. S4(a) (referred to as Q) is attributed to a quadrupolar mode. As expected, the decay of this quadrupolar mode is mostly non-radiative and does not contribute significantly to the far-field scattering.

Figure S4(c) shows the resulting spectra when we calculate the far-field emission of a *z*-oriented oscillating electric dipole ($\mathbf{p_z}$) located in the "center" and "corner" areas of the NP defined above, in the absence of the STM tip (the excitation source has a flat power spectrum).

Figure S6 shows the theoretical charge distribution on the gold nanocube under local excitation with an oscillating electric dipole at a distance of 1 nm from the cube's top face. The dipole orientation is along **z** in Figs. S6(a) and S6(b), and along **x** in Figs. S6(c) and S6(d). The dipole is located above the center of the cube's top face in all panels, except in Fig. S6(b) where the dipole is

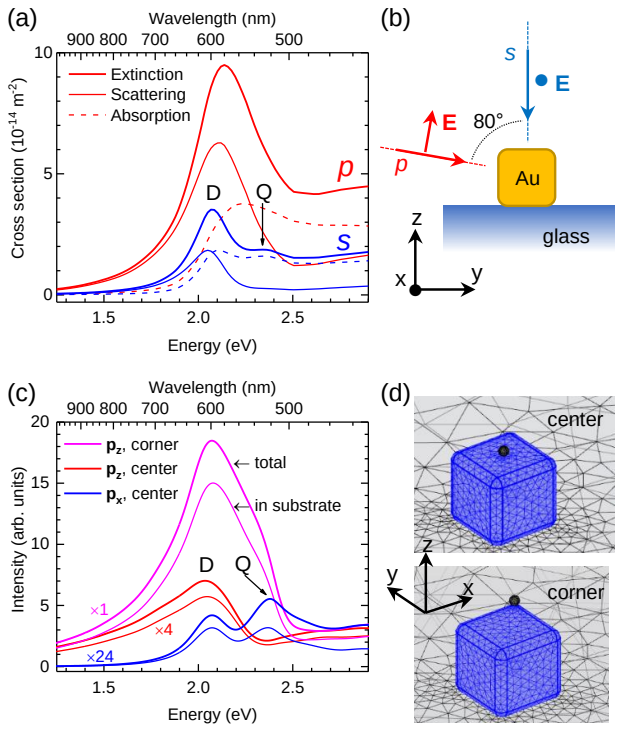

FIG. S4. "Non-local" versus "local" excitation. (a) Numerically calculated optical extinction, absorption and scattering cross sections. (b) Schematics of the model system, i.e., a gold nanocube with rounded edges on a glass substrate, under plane wave illumination (see details in the text). (c) Numerically calculated emission spectra for a vertically (**z**) or horizontally (**x**)-oriented oscillating electric dipole located 1 nm above the center or the corner of the cube's top face. Thick and thin lines correspond to the emission in the full space (4π sr) or in the substrate only (lower half-space, 2π sr). (d) Schematics of the system geometry and the mesh used in the numerical calculations for the two positions of the excitation source. Here, the presence of the STM tip is not taken into account.

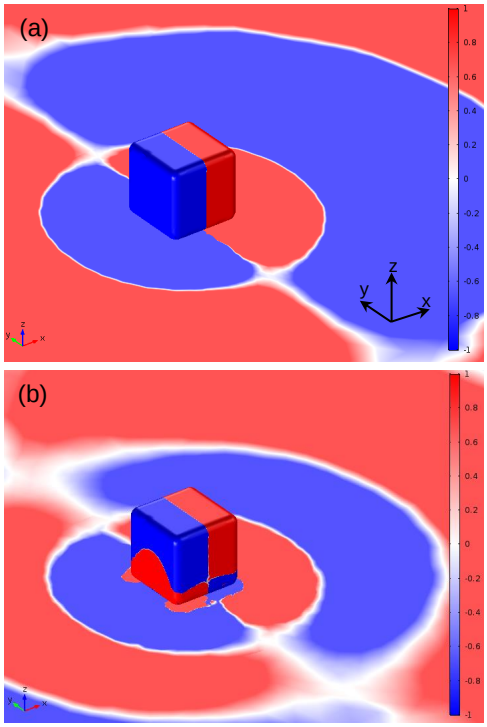

FIG. S5. Identification of the dipolar and quadrupolar modes. Numerically calculated charge distributions (in arbitrary units) on a gold nanocube under plane-wave illumination with the excitation field along **x**. Photon energy is 2.07 eV in a and 2.37 eV in b.

above its corner. The symmetry of the charge distribution is typical of a dipolar plasmon mode in Figs. S6(a) to S6(c), and of a quadrupolar mode in Fig. S6(d). Based on these charge density distributions, the dipolar (D) and quadrupolar (Q) mode contributions are identified in Figure S4(c). The emitted light in the far field is dominated by the dipolar mode of the NP along z. The density of modes at the resonance frequency of the dipolar mode along z is more than a factor of ten higher on the corner than on the center of the cube's top face. For comparison purpose, the far-field emission of an x-oriented oscillating electric dipole ($\mathbf{p_x}$) in the "center" area of the NP is also shown in Fig. S4(c). In that case, the contribution of the quadrupolar mode dominates the radiation spectrum; however, the overall radiated power is comparatively much weaker than for $\mathbf{p_z}$ at the same location. In order to compare our numerical simulations to our experimental measurements [S4–S6], we also examine the effect of considering only the light emitted in the substrate, i.e., the light that is collected using the microscope objective. For $\mathbf{p_z}$, this has no noticeable effect on the spectra other than changing its overall amplitude.

Figure S7(a) shows the results of similar calculations as in Fig. S4(c), except that the presence of the tip is now taken into account in the model. We consider a tungsten tip of simplified geometry, i.e., a cylindrical rod with a spherical end. Note the differences between the multiplying factors on the three sets of curves shown in Figs. S7(a) (×1, ×1 and ×200) and S4(c) (×1, ×4 and ×24). A comparison of these two figures reveals that the presence of the tip enhances the radiated power (i.e. its value at the energy position of the peak) by a factor of 36 for $\mathbf{p_z}$ in the "center" and by a factor of 12 for $\mathbf{p_z}$ on the "corner" areas, respectively; whereas it quenches the radiated power by a factor of 3 for $\mathbf{p_x}$. This may be explained by the polarization of the tip by the source dipole, which creates an image dipole that is oriented parallel to the source dipole for $\mathbf{p_z}$, but which is antiparallel to the source dipole for $\mathbf{p_x}$.

Figure S8 shows that the tip-induced enhancement of the radiated power in the simulation of an STML experiment depends quantitatively on the tip-sample gap size considered in the model. In this figure, results for a tip-sample gap of 1 nm (dashed line) and of 2 nm (continuous line) are plotted on two different vertical scales. The relative spectral distribution of the radiated power remains

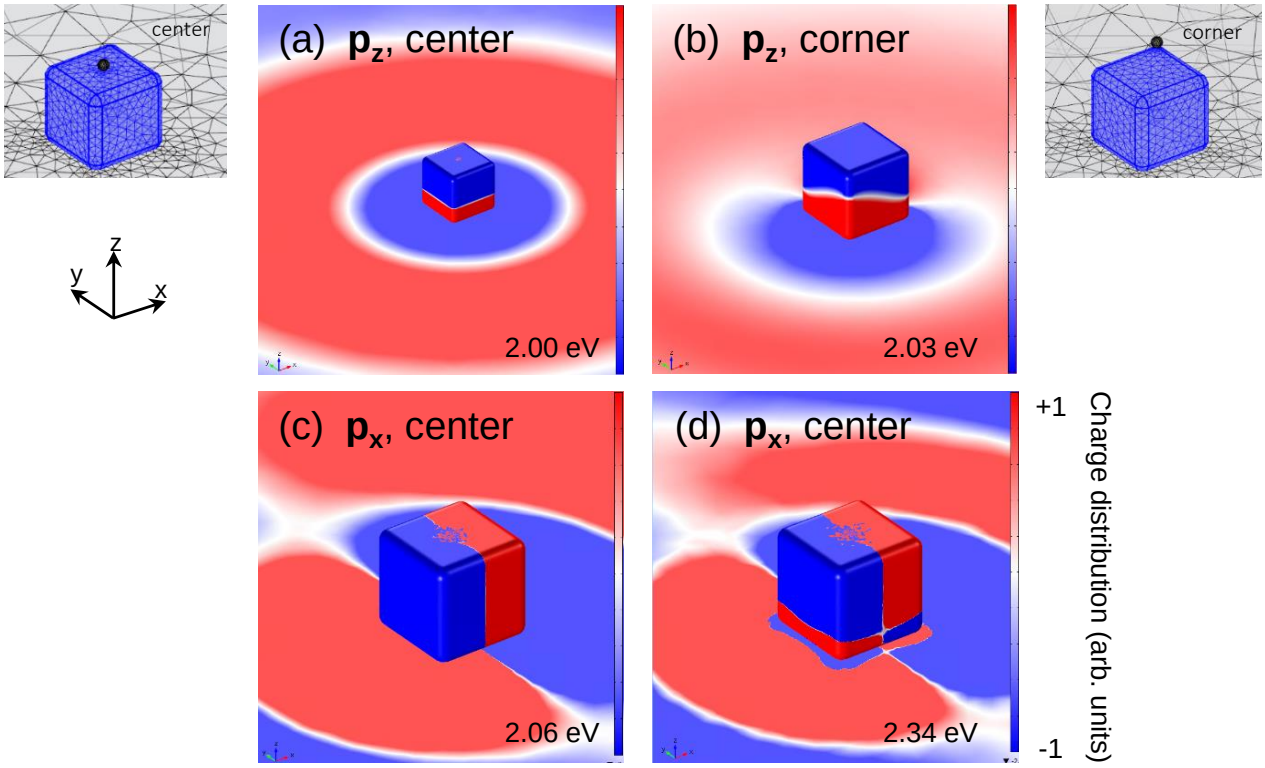

FIG. S6. Identification of dipolar and quadrupolar modes. Numerically calculated charge distributions (in arbitrary units) on a gold nanocube upon local excitation with an oscillating electric dipole at a distance of 1 nm from the cube's top face. Dipole orientation: $\mathbf{p_z}$ in a and b; $\mathbf{p_x}$ in c and d. The photon energy at which the charge distribution is numerically calculated is specified in the bottom right corner of each panels.

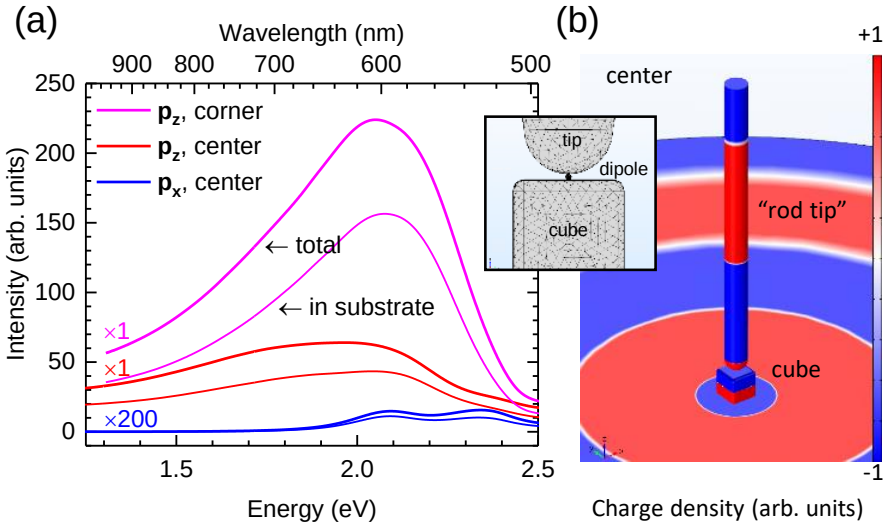

FIG. S7. Effect of the tip. (a) Similar numerical calculations as in Fig. S4(c), but including the presence of the STM tip in the simulation. (b) Charge distribution numerically calculated for the "center" position of the tip. Here, the geometry of the STM tip is simplified as a cylindrical rod that has a spherical end on the sample side and a length of 800 nm. The oscillating electric dipole is located 1 nm above the cube's top face, i.e., in the middle of the 2 nm-sized tip-sample gap.

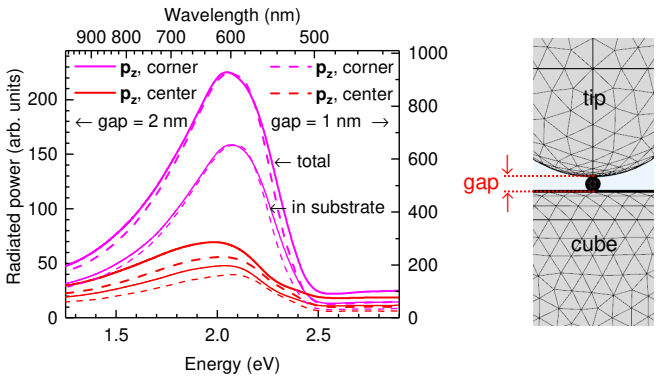

FIG. S8. Effect of the gap size. Numerically calculated emission spectra for a vertically (**z**)-oriented oscillating electric dipole ($\mathbf{p_z}$) in the middle of a 2 nm-sized tip-sample gap (left y-scale, continuous lines) or a 1 nm-sized tip-sample gap (right y-scale, dashed lines). More precisely, $\mathbf{p_z}$ is located 0.5 nm or 1 nm above the center or the corner of the cube's top face, respectively. Thick and thin lines correspond to the emission in the full space (4π sr) or in the substrate only (lower half-space, 2π sr). Right hand side of the figure: Schematics of the system geometry. The gap size is the shortest distance between the STM tip and the nanocube. The geometry of the STM tip is simplified as a cylindrical rod that has a spherical end on the sample side and a length of 800 nm.

basically unchanged (i.e., overall, the tip effect is qualitatively the same for tip-sample gaps of 1 nm and 2 nm). In other words, the tip-induced enhancement of the radiated power depends quantitatively on the tip-sample gap size considered in the model, but gap size has a negligible effect on the shape of the spectrum.

Figure S9(a) shows the spectral dependence of the total local density of electromagnetic states (EM-LDOS) [S7] numerically calculated at a point 1 nm above the center of the cube's top face and projected on the **z** axis, i.e., the direction of the tunneling current in our experiments (z-EM-LDOS). Figure S9(b) shows the same data but for the excitation located at a corner. The total EM-LDOS is related to the power transferred by the excitation source to all the modes of the system. The far-field emission spectra, on the other hand, is derived from the radiative component of the EM-LDOS. Figs. S9(a) and S9(b) compare the total EM-LDOS and the far-field emission spectra. From this data we see that most of the power emitted by $\mathbf{p_z}$ is transferred to the NP at higher energies than the resonance of its dipolar plasmon modes. This results from the extreme proximity of the excitation source to the NP. The evanescent field of the source that interacts with the NP features high spatial frequencies, which favors the excitation of higher-order multipolar modes of the NP. This is in contrast to plane wave excitation, which predominantly excites the dipolar modes. Plasmonic nanocubes support a number of higher-order multipolar modes, which do not necessarily have zero dipolar momentum, i.e., they may radiate light into free space. Due to their broad spectral width, the dipolar and higher-

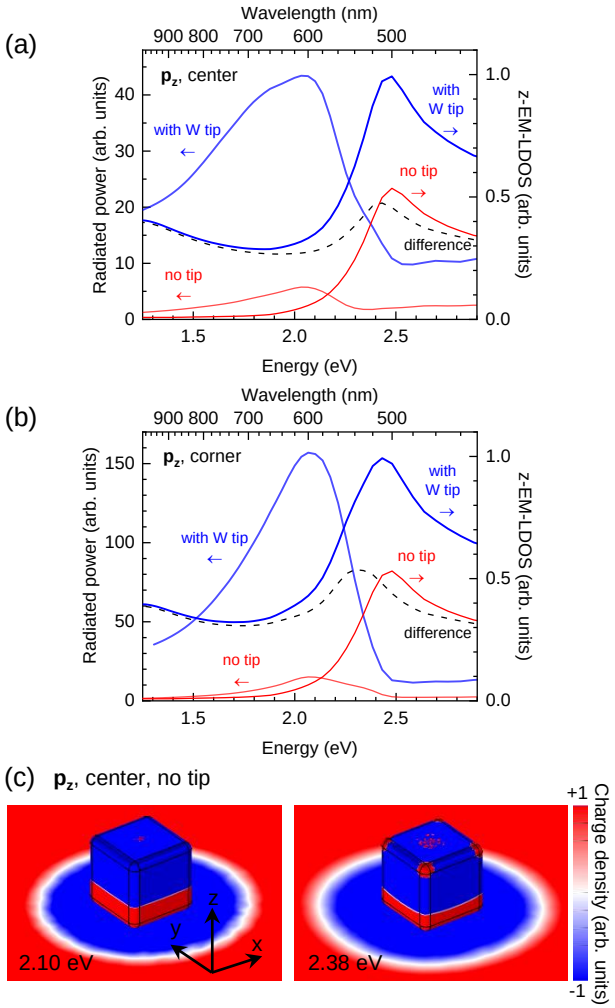

FIG. S9. The effect of a *local* excitation, revealed by the EM-LDOS and charge density distributions. [(a) and (b)] The emission spectra and the **z**-component of the total EM-LDOS are numerically calculated for a **z**-oriented oscillating electric dipole in the center (in a) and on the corner (in b) of the cube's top face in the absence and in the presence of the W tip. The dotted line labeled "difference" is the tip-induced increase of the EM-LDOS projected along the **z**-axis (z-EM-LDOS). (c) Charge density distribution numerically calculated for a **z**-oriented oscillating electric dipole in the center of the cube's top face in the absence of the tip, at two energies corresponding to the resonance of the out-of-plane dipolar and quadrupolar modes identified in Fig. S4(c).

order multipolar modes of the NP may spectrally overlap and, thus, their radiative emission may coherently interfere in the far field. In the charge density distributions shown in Fig. S9(c) (calculated at two different energies for $\mathbf{p_z}$ in the "center" of the top face, in the absence of the tip), we see a combination of the out-of-plane dipolar mode and a quadrupolar mode of the NP, which may be identified from its local charge density maxima at the four corners of the cube's top face. From this, we infer that the Fano-like profiles [S8] of the radiation power

spectra of $\mathbf{p_z}$ shown in Figs. S9(a) and S9(b) result from the far-field interference of the dipolar and quadrupolar modes [see also D and Q in Fig. S4(c)]. In particular, on the high-energy side of the dipolar resonance, the two modes interfere destructively for $\mathbf{p_z}$ in the "center" and constructively for $\mathbf{p_z}$ on the "corner". Globally, for $\mathbf{p_z}$ in the "center", the interaction of the dipolar and quadrupolar modes broadens the radiation power spectrum on the low-energy side and narrows it on the high-energy side, which yields an apparent red-shift as compared to the scattering cross section of the NP; whereas, this effect is not observed for $\mathbf{p_z}$ on a "corner". Indeed, at a given oscillation frequency, the lateral position of the tip on the NP's top face determines the phase relationship between the excited plasmon modes.

Figures S9(a) and S9(b) also show the effect of the tip. The presence of the tip yields an increase in the z-EM-LDOS, i.e., the EM-LDOS projected along the **z**-axis. This increase is similar to the addition of a "vertical" offset (i.e., a flat background) to the z-EM-LDOS that is obtained in the absence of the tip (see the "difference" curve represented by a dotted line). This "vertical" offset results from the polarization of the tungsten tip, i.e., the creation of an image dipole, whose amplitude varies little within the investigated frequency range because tunsgten is a non-plasmonic material and the real part of its permittivity is high compared to that of the surrounding medium (i.e., air). Moreover, Figs. S9(a) and S9(b) show that, on the *low-energy* side of the dipolar resonance, the contribution of the tip to the total z-EM-LDOS strongly dominates over that of the NP, which is not true on the *high-energy* side of the dipolar resonance. This naturally explains why the presence of the tip further redshifts and broadens the emission peak.

For the modelling of the STM tip in the simulations, we have used the radius of curvature determined from electron micrographs of tungsten tips prepared using the same protocol as for the tungsten tips used to measure the STML spectra, i.e., a radius of curvature equal to 30 nm [S4]. Nevertheless, in order to evaluate the impact of the tip/nanoparticle size ratio on the simulated STML spectra, we have carried out additional simulations for various radii of curvature of the tip, ranging from 30 nm to 5 nm. Figure S10 shows the results of these calculations. The simulations have been carried out in the absence of the water bridge, in order to distinguish the effect of the tip size from the effect of the size of the water bridge. We observe that the simulated STML peaks are redshifted with respect to the simulated scattering spectrum of the NP even when a tip with a radius of curvature as small as 5 nm is considered in the STML simulations. We also observe that increasing the radius of curvature of the STM tip yields a larger broadening of the STML peaks on the lower-energy side; however, this effect cannot explain the much larger redshift of the STML peaks observed in the presence of the water bridge.

In the simulations where the presence of a water bridge is taken into account, we assumed that the water bridge has the same radius as the cylinder used to model the STM tip, i.e., 30 nm. In order to examine the influence of this assumption, we have carried out simulations for various radii of the water bridge, ranging from 30 nm to 5 nm, while keeping the radius of curvature of the tip equal to 30 nm. The results of these calculations are shown in Figure S11(a). We observe that, within the investigated range (i.e., 5 to 30 nm), the radius of the water bridge has a negligible effect on the simulated STML spectra, which confirms our assumption that the geometry of the water bridge has virtually no influence on the conclusions of our study. In order to explain the absence of this influence, we have simulated the spatial distribution of the electric field in the tip-sample gap in the presence of the water bridge. The results are shown in Figure S11(b). We observe that the electric field is essentially confined within a nanoscopic region around the excitation source that is in the center of the tip-sample junction. As a result, the simulated STML spectra are most sensitive to the dielectric permittivity of the medium bridging the tip-sample gap within this nanoscopic region where the electric field in concentrated, and are much less sensitive to the permittivity in regions further from the position of the excitation source. Based on these simulations of the electric field, we estimate that this nanoscopic region has a lateral extend of only a few nanometers, which explains why the simulated STML spectra calculated for radii of the water bridge varying from 5 to 30 nm are almost identical.

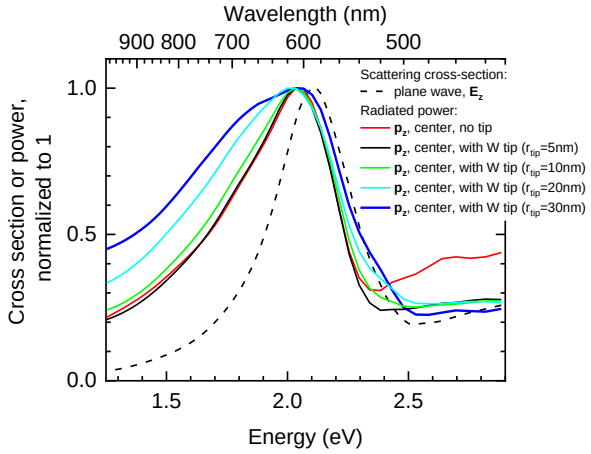

FIG. S10. Numerical simulations of the energy shifts and peak broadening due to tip and near-field excitation effects: Influence of the radius of curvature of the tip. Scattering cross section of a nanocube for p-polarized illumination (dashed lines) and emission spectra for a **z**-oriented oscillating electric dipole located in the center of the cube's top face in the absence (red line) and in the presence of the tungsten (W) tip for various radii of curvature of the tip, ranging from 30 nm (blue line) to 5 nm (black line). All curves are normalized with respect to their maximum value.

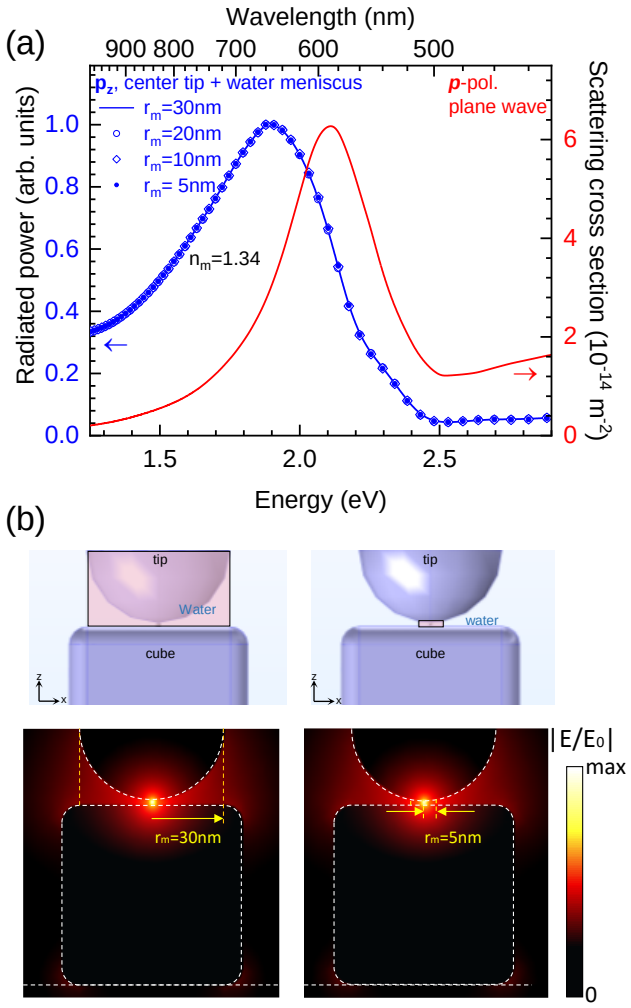

FIG. S11. The effect of the radius of the water bridge. (a) Simulated emission spectra for a vertically (**z**)-oriented oscillating electric dipole located 1 nm above the center of the cube's top face, in the absence (red line) and in the presence of the tungsten tip and water bridge, calculated for various radii of the water bridge, ranging from 30 nm to 5 nm, while keeping the radius of curvature of the tip equal to 30 nm (blue line and dots). (b) Geometry of the water bridge considered in the calculations and simulated spatial distribution of the electric field in the tip-sample gap in the presence of the water bridge, calculated for radii of the water bridge equal to 30 nm (left) and 5 nm (right).

[S1] M. Haggui, M. Dridi, J. Plain, S. Marguet, H. Perez, G. C. Schatz, G. P. Wiederrecht, S. K. Gray, and R. Bachelot, Spatial confinement of electromagnetic hot and cold spots in gold nanocubes, ACS Nano **6**, 1299 (2012).

[S2] C. Deeb, X. Zhou, R. Miller, S. K. Gray, S. Marguet, J. Plain, G. P. Wiederrecht, and R. Bachelot, Mapping the electromagnetic near-field enhancements of gold nanocubes, J. Phys. Chem. C **116**, 24734 (2012).

[S3] J. Deumer, B. R. Pauw, S. Marguet, D. Skroblin, O. Taché, M. Krumrey, and C. Gollwitzer, Small-angle X-ray scattering: characterization of cubic Au nanoparticles using Debye's scattering formula, J. Appl. Crystallogr. **55**, 993 (2022).

[S4] E. Le Moal, S. Marguet, B. Rogez, S. Mukherjee, P. Dos Santos, E. Boer-Duchemin, G. Comtet, and G. Dujardin, An electrically excited nanoscale light source with active angular control of the emitted light,

Nano Lett. **13**, 4198 (2013).

[S5] E. Le Moal, S. Marguet, D. Canneson, B. Rogez, E. Boer-Duchemin, G. Dujardin, T. V. Teperik, D.-C. Marinica, and A. G. Borisov, Engineering the emission of light from a scanning tunneling microscope using the plasmonic modes of a nanoparticle, Phys. Rev. B **93**, 035418 (2016).

[S6] S. Cao, M. Zapata-Herrera, A. Campos, E. Le Moal, S. Marguet, G. Dujardin, M. Kociak, J. Aizpurua, A. G. Borisov, and E. Boer-Duchemin, Probing the radiative electromagnetic local density of states in nanostructures with a scanning tunneling microscope, ACS Photonics **7**, 1280 (2020).

[S7] K. Joulain, R. Carminati, J.-P. Mulet, and J.-J. Greffet, Definition and measurement of the local density of electromagnetic states close to an interface, Phys. Rev. B **68**, 245405 (2003).

[S8] S. Zhang, K. Bao, N. J. Halas, H. Xu, and P. Nordlander, Substrate-induced Fano resonances of a plasmonic nanocube: A route to increased-sensitivity localized surface plasmon resonance sensors revealed, Nano Lett. **11**, 1657 (2011).